Bedrock Offset Across the Wasatch Fault in Salt Lake City, Utah, from Teleseismic Converted Phases and Its Geologic Implications

HyeJeong Kim[*1,2], James C. Pechmann[1], Fan-Chi Lin[1], Adam P. McKean[3], and Christian L. Hardwick[3]

Abstract

In 2018, 32 three-component geophones were deployed in a linear array with ~90 m average station spacing across the active East Bench fault (EBF) in Salt Lake City, Utah. This west-dipping normal fault is a relatively young section of the Wasatch fault zone which cuts through the northeastern Salt Lake basin (SLB), west of and mostly parallel to the older Foothill fault section at the base of the Wasatch Range. Here, we investigate the variation of bedrock depth across the fault by examining the first peak of teleseismic receiver functions (RFs) along the linear array. The arrival time of this initial phase at stations in the SLB is particularly sensitive to the depth of a velocity discontinuity, referred to as R2, between semi-consolidated sediment and bedrock, which is consolidated sedimentary rock in most of the SLB. We observe that the first peak times are very similar on either side of the EBF but shift abruptly by ~0.7 s across the fault. Based on two recent 1D velocity models, one for each side of the fault, this time shift indicates a vertical R2 offset of 810 ± 290 m across the EBF. This offset likely reflects the accumulated slip on the fault since the fault's activation. Combining this offset with a current slip rate of 1.2 ± 0.2 mm/yr, based on paleoseismic studies of the Wasatch fault, and a range of models for how this slip rate may have changed over time, our best estimate for the age of the EBF is 0.7–1.4 Ma. From the R2 offset and the distance between stations over which it is observed, we calculate that the EBF has a minimum average dip of 81° ± 3° in the top 1100 m.

Cite this article as Kim, H.J., J. C. Pechmann, F.-C. Lin, A. P. McKean, and C. L. Hardwick (2025). Bedrock Offset Across the Wasatch Fault in Salt Lake City, Utah, from Teleseismic Converted Phases and Its Geologic Implications, *Seismol. Res. Lett.* **XX**, 1–10, doi: 10.1785/0220250236.

Supplemental Material

Introduction

The Wasatch fault zone (WFZ) is a west-dipping normal fault zone on the western edge of the Wasatch Range, which forms the boundary between physiographic provinces of the Basin and Range to the west and the Middle Rocky Mountains and Colorado plateau to the east (Fig. 1a). The WFZ has been active since 12 ± 2 Ma (Ehlers *et al.*, 2003) to ~18 Ma (Parry and Bruhn, 1987), which is the middle Miocene. This fault is the largest source of the elevated earthquake hazard across the Wasatch Front region of north-central Utah (Petersen *et al.*, 2014, 2024; Wong *et al.*, 2016). Understanding the fault geometry and slip rate of each fault segment is critically important for constructing earthquake rupture scenarios and estimating earthquake recurrence intervals (Wong *et al.*, 2016; Petersen *et al.*, 2014, 2024). Although paleoseismic trenching provides direct evidence of fault parameters near the surface (e.g., DuRoss *et al.*, 2016), obtaining constraints on fault displacement and geometry at depths beyond several meters remains challenging. In addition, there are practical difficulties with conducting paleoseismic trenching in an urban area.

The East Bench fault (EBF) in the northeastern Salt Lake basin (SLB) is part of the Salt Lake City segment of the WFZ (Fig. 1a). The EBF lies west of and runs roughly parallel to the Foothill fault (FF), which is an older range-bounding fault along the northern Salt Lake segment. The EBF "stepped out" to the west from the FF relatively recently in the history of the WFZ and has now replaced the FF as the primary active trace of the WFZ in the northeastern SLB (Marsell, 1969; Scott

1. Department of Geology and Geophysics, University of Utah, Salt Lake City, Utah, U.S.A., https://orcid.org/0000-0002-8271-4319 (HJK); https://orcid.org/0000-0002-6726-9640 (JCP); https://orcid.org/0000-0003-0394-6830 (F-CL); 2. Now at Université Côte d'Azur, Observatoire de la Côte d'Azur, CNRS, IRD, Géoazur, Valbonne, France; 3. Utah Geological Survey, Salt Lake City, Utah, U.S.A., https://orcid.org/0000-0002-0207-4340 (CLH)

*Corresponding author: hkim.geo@gmail.com; hyejeong.kim@utah.edu

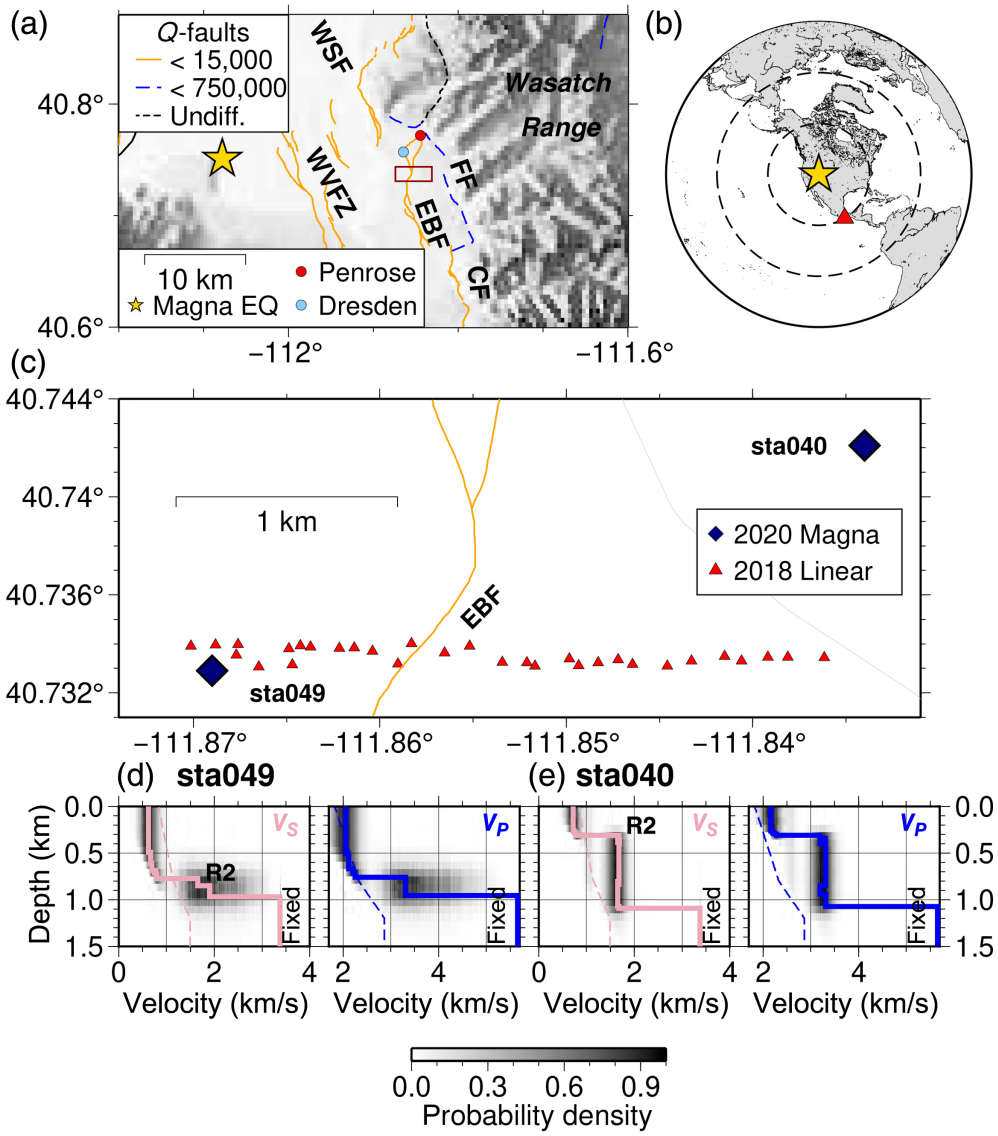

Figure 1. An overview of the data used in this study. (a) The tectonic setting of the study area (red box). The yellow star marks the epicenter of the 18 March 2020 M_w 5.7 Magna earthquake. The red and blue circles mark the locations of the Penrose Drive (DuRoss *et al.*, 2014) and Dresden Place (Garr, 1986) trenching sites, respectively. The major Quaternary faults ("Q-faults"; U.S. Geological Survey and Utah Geological Survey, 2023) are shown in different line types and colors according to their age of most recent movement, as indicated in the key; their names are abbreviated as follows: CF, Cottonwood fault; EBF, East Bench fault; FF, Foothill fault; WSF, Warm Springs fault; WVFZ, West Valley fault zone. (b) The locations of the teleseismic event used for the receiver function (RF) analysis (red triangle) and the Magna earthquake (yellow star). The dashed circles mark 30° and 60° epicentral distances from the location of the array. (c) Map of the area of the red box in (a) showing the distribution of stations used for the RF analysis as red triangles and the surface trace of the EBF. The two dark blue diamonds mark the locations of stations that provided the velocity models for migration, determined by Kim *et al.* (2025; Fig. S2) from joint inversion of RFs and Rayleigh-wave data. McKean's (2020) geologic map of this area shows colluvium and alluvial fan deposits on the western side of the EBF, with alluvial fan deposits plus lacustrine silt and clay from Lake Bonneville on the eastern side. (d) The velocity model beneath station sta049, used to represent the hanging wall, and (e) the velocity model beneath station sta040, used to represent the footwall, in the RF migration. The thin dashed lines are the V_P and V_S velocity models simplified from the WFCVM (Magistrale *et al.*, 2008). Stations sta040 and sta049 were deployed in 2020 by Allam (2020). The color version of this figure is available only in the electronic edition.

and Shroba, 1985; Machette *et al.*, 1992; Personius and Scott, 1992). The FF offsets pre-Lake Bonneville deposits (Early–Middle Pleistocene) along its northern extent, but no evidence for Holocene ruptures on this fault has been reported (McKean, 2020; Anderson *et al.*, 2024). In contrast, a paleoseismic investigation on the northern end of the EBF found that five Holocene surface-faulting earthquakes had occurred at this site and determined a latest Pleistocene and Holocene vertical slip rate of 0.5–0.9 mm/yr (DuRoss *et al.*, 2014; DuRoss and Hylland, 2015). The exact timing of the slip transfer from the FF to the EBF is unknown, and it may not yet be complete. Both faults are included as seismic sources in the 2023 National Seismic Hazard Model (Hatem *et al.*, 2022).

Ambient noise surface-wave studies have demonstrated the possibility of imaging fault zone structures using dense arrays (Wang *et al.*, 2021; Biondi *et al.*, 2024). In the SLB, Gkogkas *et al.* (2021) inverted Rayleigh-wave phase velocity measurements between 0.4 and 1.1 s period from a dense linear array across the EBF (Fig. 1c). They found an asymmetric low-velocity anomaly near the surface trace of EBF that they interpreted as a fault damage zone. Although surface-wave dispersion measurements do not have the resolution to resolve sharp vertical velocity changes, their results indicate a sedimentary layer that is ~300 m thick east of the EBF and gradually thickens toward the west. On the west side of the EBF, the top of the bedrock is deeper than the resolution

depth (<400 m) of their study, based on the results of Kim *et al.* (2025) (e.g., Fig. 1d).

In comparison to surface-wave measurements, *P*-to-*S* converted phases (i.e., the *Ps* phase) from teleseismic earthquakes are more sensitive to vertical velocity discontinuities and have been employed to improve constraints on the structure of sedimentary basins (e.g., Agostinetti *et al.*, 2018; Berg *et al.*, 2021; Agrawal *et al.*, 2022). These teleseismic converted phases are analyzed using the receiver function (RF) method. An RF is the radial component record of a teleseismic *P*-wave arrival from which the vertical component record has been deconvolved to remove the source time function and obtain the near-receiver seismic response (Langston, 1979). Where there is a low-velocity sediment layer at the surface, the *P*- and *S*-wave ray paths are refracted to nearly vertical. Hence, the first significant peak in the RF is usually the *Ps* phase generated at the base of the layer, which arrives later than the first peak in the vertical component (i.e., the *P* wave).

In our recent study of the entire SLB, stations located on the sedimentary basin fill showed significant time delays in RF peaks (Kim *et al.*, 2025). We jointly inverted the RF initial peak waveform, the Rayleigh wave ellipticity (Rayleigh wave H/V; Zeng *et al.*, 2022), and the Rayleigh-wave phase velocity at each station to obtain a set of station-specific 1D shear-wave velocity (V_S) profiles in the SLB. These inverted velocity models confirm that the first peak in the RFs mostly corresponds to the *Ps* phase generated at a strong impedance contrast within the SLB referred to as R2. We note that in some areas with multiple near-surface impedance contrasts, the RF maximum peak can be the *PpPs* phase, a multiple that crosses a seismic discontinuity as a *P* wave, reflects off the surface, and then converts to an upgoing *S* wave at the discontinuity (Zhu and Kanamori, 2000; Kim *et al.*, 2025).

R2 is the strongest of three prominent seismic reflectors within the SLB that Hill *et al.* (1990) identified on seismic reflection data, sonic logs, and density logs from the northern Salt Lake Valley and named R1, R2, and R3 in order of increasing depth. Following Arnow and Mattick (1968) and Mattick (1970), Hill *et al.* (1990) interpreted these reflectors to be the boundaries separating the following four generalized geologic units: unconsolidated Quaternary sediments, semi-consolidated Tertiary sediments, Tertiary sedimentary and volcanic bedrock, and older basement rocks. All the units above R3, the top of the basement rocks, were deposited in the SLB as it formed due to downward movement along the Wasatch fault (Mattick, 1970; Hill *et al.*, 1990). Kim *et al.*'s (2025) model reveals >1 km of lacustrine and alluvial deposits above R2 within an intra-basin graben between the west-dipping EBF to the east and the east-dipping antithetic West Valley fault zone (WVFZ) to the west (Fig. 1a; DuRoss and Hylland, 2015; Zeng *et al.*, 2022). Note that R2, the boundary between semi-consolidated Tertiary sediments and the underlying Tertiary sedimentary and volcanic bedrock, is a lithification horizon. Because the degree to which sediments are lithified depends on both their age and depth of burial, and the rate of subsidence varies across the SLB, R2 is not necessarily the same age everywhere. We are not aware of any precise dates for the R2 horizon anywhere in the SLB. However, volcanic tuffs and ashes from western Salt Lake Valley exposures of the Salt Lake Formation, which may be correlative with the younger rocks between R2 and R3 in the SLB, range in age from 4.4 ± 1.0 Ma to 6.6 Ma (Clark *et al.*, 2020). The oldest rocks between R2 and R3 in the SLB would be those formed from sediments deposited shortly after the WFZ became active at 12 ± 2 Ma to 18 Ma (Ehlers *et al.*, 2003; Parry and Bruhn, 1987).

Although Hill *et al.*'s (1990) four-layer basin model was developed for the SLB, this basic model appears to apply to other extensional basins in the Wasatch Front region based on limited sonic log and seismic reflection data (Magistrale *et al.*, 2008; Pechmann *et al.*, 2010; Stephenson *et al.*, 2012). Sonic logs from the region show that R2 is clearly the largest of the three velocity discontinuities of Hill *et al.* (1990) and is the only one that is easily identifiable on these logs without lithologic information. The sharp *P*-wave velocity increase at R2 takes place over a vertical distance of 20–100 m, depending on the location and how the bounds of the velocity increase are defined (Hill *et al.*, 1990; Pechmann *et al.*, 2010). These observations, in combination with the modeling of Kim *et al.* (2025), give us confidence that the *Ps* phase that we identify in our receiver functions is generated at the R2 discontinuity.

In this study, we analyze RFs of the dense linear array across the EBF (Fig. 1c) to investigate with high lateral resolution the variation of bedrock depth (i.e., R2) across the fault. Because we do not have surface-wave measurements along the linear array that are sensitive to structure below 400 m depth to facilitate V_S model inversions, we migrate the time-domain RFs into the depth domain (Dueker and Sheehan, 1997) using existing velocity models. We use two 1D velocity models from our recent study (Kim *et al.*, 2025), one velocity model on each side of the EBF, to account for shallow velocity differences between the footwall and hanging wall (Fig. 1d,e). We show that our approach resolves sharp sediment thickness changes across the EBF, which enables us to determine a minimum near-surface dip on this fault and the amount of vertical fault displacement accumulated since its activation. Furthermore, this displacement, combined with estimates of the current slip rate on the Salt Lake City segment and some assumptions about the transfer of slip from the FF to the EBF, allows us to evaluate the timing of the initiation of slip on the EBF. This EBF age estimate adds to our knowledge of how the Wasatch fault has changed and evolved with time.

Data and Methods

RF analysis along the linear array

For the RF analysis, we utilized three-component 5-Hz geophones that were deployed for approximately a month starting in early February of 2018 (Lin and Kim, 2018). The east–west linear array consisted of 32 stations distributed along a 2.9 km

section of 1700 South Street that crosses the EBF (Fig. 1c). We found two candidate RF events in the U.S. Geological Survey Preliminary Determination of Epicenters (PDE) catalog that occurred during the time of operation of the array and also met our other criteria, namely an epicentral distance between 25° and 90° and a magnitude ≥ 6.0. To compute an RF, we deconvolved the vertical component from the radial component of a teleseismic *P*-wave record using the extended time multi-taper correlation method (Shibutani *et al.*, 2008). For the deconvolution, we used time windows relative to the theoretical *P*-wave arrival time of −35 to +102.5 s for the signal and −135 to −35 s for the pre-signal noise. The RFs were Gaussian low-pass filtered ($e^{-\omega^2/4a^2}$) with $\boldsymbol{a} = 3.5$, which corresponds to a corner frequency of ∼0.81 Hz. We imposed two criteria for quality assurance. First, the signal-to-noise ratios (SNRs) for both the radial- and vertical-component waveforms should be larger than $\sqrt{2.5}$. Here, we define the noise and signal windows as the time between −80 and −10 s and −10 and 60 s relative to the expected *P*-wave arrival time, respectively. The SNR was measured by taking the root mean square ratio between the signal and noise windows, after removing the instrument response and band-pass filtering between 0.1 and 1.0 Hz. The second criterion is that the RFs should have an SNR greater than 1.0 to discard RFs affected by deconvolution instabilities.

Of the two teleseismic events, only the 16 February 2018 M_w 7.2 southern Mexico earthquake provided RFs that passed the SNR criteria (Fig. 1b). All the RFs from this teleseism have an SNR > 1.30, except for one with SNR = 1.18, and 77% are above 1.50. The majority (∼75%) of the radial- and vertical-component SNRs are above 2.7 and 4.3, respectively (Fig. S1, available in the supplemental material to this article). This teleseismic event has a back azimuth of ∼150°, which is roughly parallel to the strike of the southern EBF (Fig. 1a). Hence, the radial RFs should be minimally affected by scattered seismic energy from the fault zone.

We measured the time delay of the first peak of the RF by measuring the time of the RF's maximum amplitude within the time interval −1 to +2 s (Fig. 2, Fig. S1b). Because there is no other positive peak that precedes the first peak, we interpret this peak as the *P*-to-*s* converted phase from the R2 discontinuity. Benefiting from the dense station spacing of ∼90 m (Fig. 1c), and the fact that an RF is only sensitive to structure right beneath the station (especially in slow shallow velocity areas), the 2018 linear array can resolve R2 depth changes with high horizontal spatial resolution.

Migration of RFs to depth

We migrated the time-domain RFs into the depth domain (Gurrola *et al.*, 1994; Dueker and Sheehan, 1997) by employing velocity models from the seismic data inversions by Kim *et al.* (2025) (Fig. 1d,e, Fig. S2). The migration assumes that each point in the time-domain RF corresponds to a *Ps* phase converted at some depth. We used two 1D velocity models to migrate the RFs, one for stations on the west (hanging-wall) side of the fault (Fig. 1d) and the other for stations on the east (footwall) side (Fig. 1e). We used only the part of each velocity model that is above the R2 interface ($V_S < 1.5$ km/s) and inserted an underlying half-space. We note that the elevations of the migrated RF first peaks do not change significantly when using different cutoff frequencies for the Gaussian low-pass filter (Fig. 3c). Hence, the possibility that the first RF peaks consist of mixed *Ps* and *PpPs* phases instead of *Ps* only can be disregarded (e.g., Cunningham and Lekic, 2019). Next, we calculate the difference between the average elevations of the maximum first peak amplitudes, which we interpret as R2, on each side of the fault to obtain the R2 displacement. Here, we use sea level as the reference elevation because the surface elevation along the array decreases westward.

The accuracy of the migration results depends on the accuracy of the 1D velocity models. To estimate the uncertainty in the R2 displacement, we also migrated the RFs using the ensembles of 1D velocity models that come from the Bayesian inversions of Kim *et al.* (2025; Fig. 1d,e). We converted the posterior distributions of the two velocity models into two distributions of average R2 elevations, one for the hanging wall (Fig. S3a) and one for the footwall (Fig. S3b). Then, we randomly selected a mean R2 elevation from each distribution and calculated the difference. Repeating the last step 20,000 times, we obtained a distribution of R2 displacements (Fig. S3c) from which we computed the standard deviation (Table 1, Fig. 2d).

To further investigate the sensitivity of the calculated R2 displacement to the velocity models, we also migrated the RFs using two other velocity models. The first model is a simplified version of the Wasatch Front Community Velocity model (WFCVM; Magistrale *et al.*, 2008), consisting of the velocity gradients used in this model between the R1 and R2 discontinuities and constant velocities below 1200 m (dashed lines in Fig. 1d,e). The WFCVM between R1 and R2 was constructed from sonic log data and an empirical relation between *P*- and *S*-wave velocities (V_P and V_S, respectively). The second model is a hybrid velocity model consisting of the ambient noise tomography model of Gkogkas *et al.* (2021) from 0 to 400 m depth and the simplified WFCVM below this depth.

Results

RF first peak time variation across the EBF

Observed RF peak delay times increase sharply by ∼0.7 s from east to west across the EBF (Fig. 2a,b). The increase occurs over a short distance (≤157 m) between stations on opposite sides of the fault, as seen in the map view (Fig. 2a) and in the time-domain RFs (Fig. 2b). The sharp lateral change in RF peak delay times demonstrates that the RFs provide outstanding lateral resolution of the R2 elevation variations. This result is consistent with previous RF studies, which have demonstrated that RFs have the capability to resolve lateral discontinuity

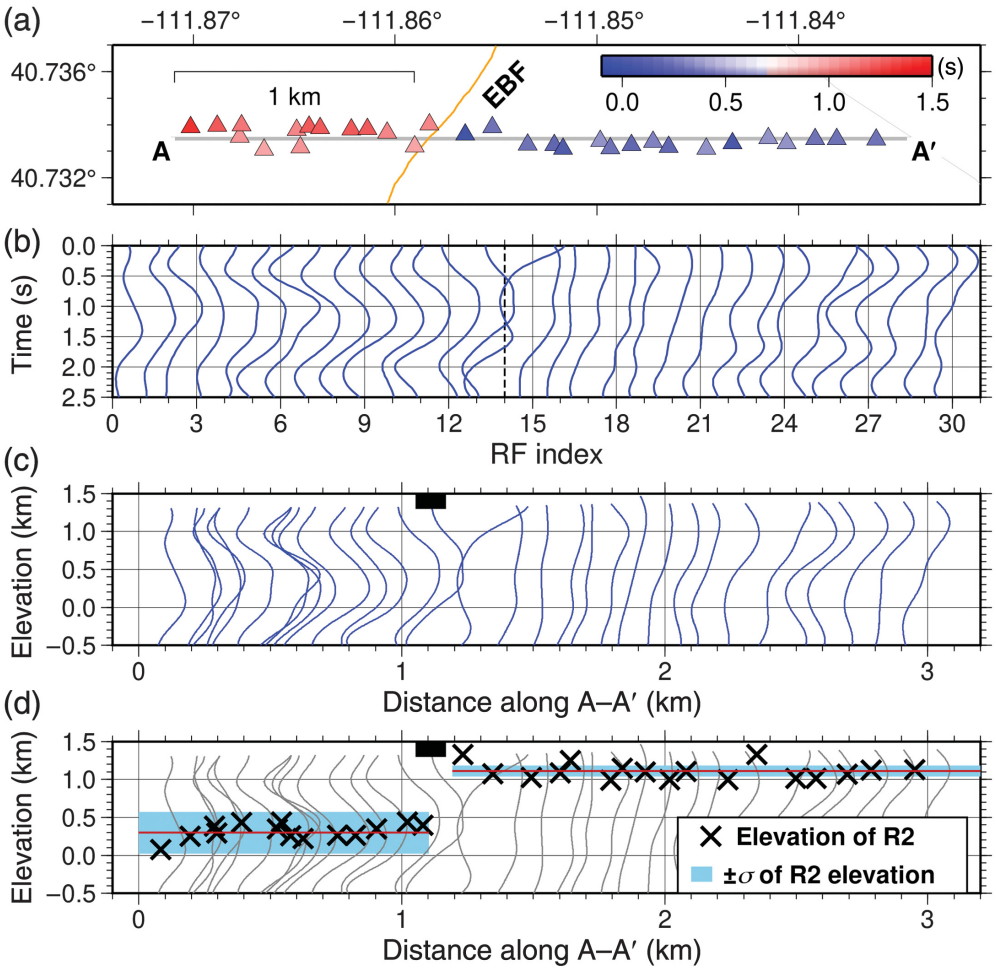

Figure 2. Observed RFs for the stations in the linear part of the array in Figure 1c. (a) Map view of the stations and the surface trace of the EBF. The colors show RF peak delay times as indicated by the color map in the upper right. (b) The time domain RFs, aligned in order from west to east along the A–A′ profile in (a). The vertical dashed line marks the surface trace location of the EBF relative to the station indices. (c) RFs migrated to depth using the velocity models for the footwall and hanging wall indicated by the thick solid lines in Figure 1d,e, respectively. The RFs are plotted at the projections of their corresponding station locations onto the A–A′ profile in (a). Elevations are relative to sea level. The solid black box on this profile and the one below it marks the location of the EBF surface trace. (d) Depth-migrated RFs, with the elevations of the RF peaks marked by black crosses at the projections of the station locations on the cross-section. The red thin lines show the average elevations of the crosses, which we interpret as R2 elevations, in the hanging wall (left; west) and the footwall (right; east) of the EBF. The light blue shading marks the $\pm 1\sigma$ range of the mean R2 elevations.

variations smaller than the Fresnel zone half-width, particularly at shallow depths (e.g., Lekić and Fischer, 2017). For reference, the Fresnel zone half-width for *P*-to-*s* RFs with an ∼1 Hz cut-off frequency ($\boldsymbol{a}$ = 3.5) at ∼1.0 km depth, based on the velocity structure in Figure 1d, is approximately 1.7 km. For this velocity structure and the teleseism that we used to compute our RFs, the horizontal offset of a *Ps* ray path between a 1.0 km deep R2 discontinuity and the ground surface is ∼56 m. This short offset distance, in combination with the ∼150° back azimuth of the teleseism, suggests that the piercing points of *P*-to-*s* converted phases recorded by stations closest to the fault are on the same side of the fault as the station.

R2 depths across the EBF

Similar to the shift of RF time delays across the fault, the migrated RFs show a clear R2 elevation change across the fault (Fig. 2c). The average R2 elevations on the hanging wall and footwall (red lines in Fig. 2d), rounded to the nearest 10 m with one standard deviation error bars, are 300 ± 280 m and 1110 ± 70 m, respectively. These elevations differ by 810 ± 290 m (Table 1). The small variations in R2 depths on both sides of the fault (Figs. 2d and 3c) are probably at least partially due to small-scale velocity variations that are not accounted for by our two reference velocity models (Fig. 1d,e).

Using different velocity models for the migration results in different R2 elevations (Fig. 3a,b). Migration with the simplified WFCVM results in a much deeper R2 (Fig. 3a) on both sides of the fault and a larger R2 offset of 1420 m. The deeper R2s are due to the lower V_P/V_S ratios in the WFCVM compared to our preferred reference models (Kim *et al.*, 2025). The R2 displacement from the migration with Gkogkas *et al.*'s (2021) model is 719 m (Fig. 3b), which falls within the uncertainty range of our preferred estimate. However, Gkogkas *et al.*'s (2021) model produces more variability in the R2 elevation on the hanging-wall side than the other models. For example, a ∼500 m deepening of the R2 elevation is observed around X = 0.7 km when using the Gkogkas *et al.* (2021) model (Fig. 3b), whereas this deepening is less prominent when using the other velocity models (Fig. 3). This difference reflects the small-scale lateral velocity variations present in the 2D velocity model of Gkogkas *et al.* (2021), which are not present in the other velocity models (Fig. 1d,e).

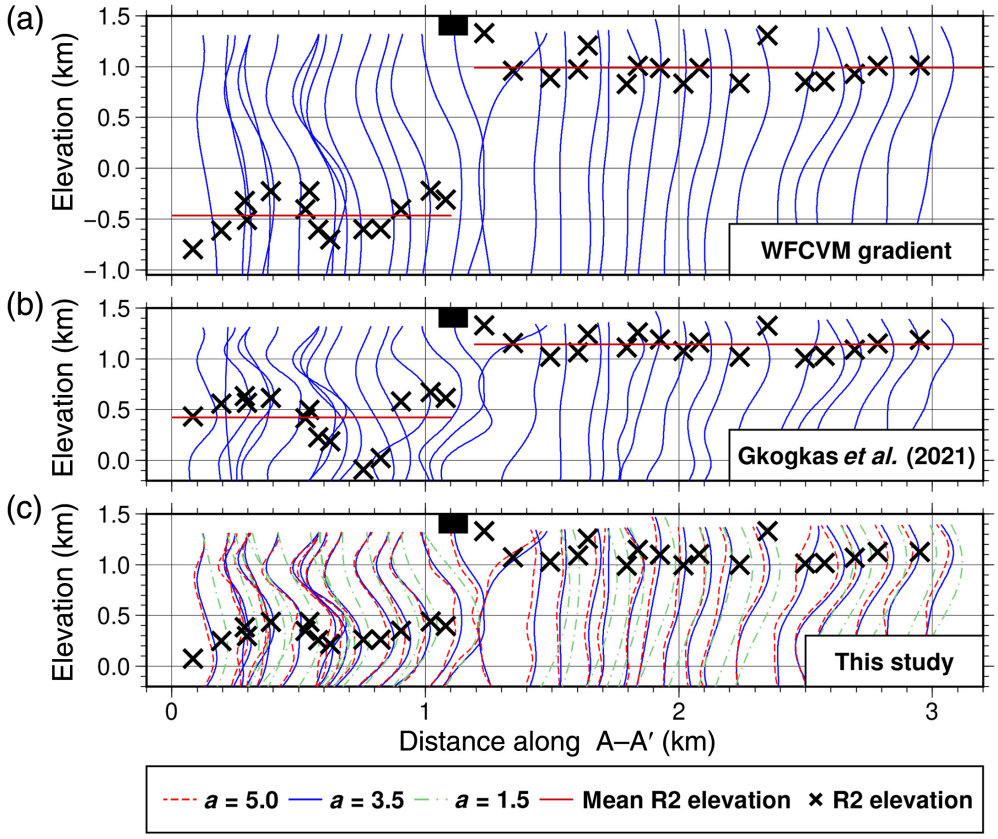

Figure 3. Depth migrated RFs using different velocity models: (a) the modified WFCVM (dashed lines in Figs. 1d,e; Magistrale *et al.*, 2008); (b) Gkogkas *et al.*'s (2021) velocity model, extended below its maximum depth of 400 m from the surface by combining with the modified WFCVM; and (c) the models in Figures 1d,e. The black crosses are the R2 elevations determined from the RFs. The thin red solid lines show the average elevations of the crosses in the hanging wall (left; west) and the footwall (right; east) of the EBF. In (c), the different line types denote RFs constructed using different values of the Gaussian low-pass filter ($e^{-\omega^2/4a^2}$) parameter ***a***. The red dashed, blue solid, and green dashed–dotted lines denote ***a*** values of 5.0, 3.5, and 1.5, respectively, which correspond to cut-off frequencies of approximately 1.3, 0.81, and 0.35 Hz. The black crosses are the R2 elevations determined using RFs filtered with parameter ***a*** = 3.5, as in Figure 2d. The solid black boxes at ~1.1 km along the A–A′ profiles in (a), (b), and (c) mark the location of the EBF surface trace. The color version of this figure is available only in the electronic edition.

Discussion

We utilize our estimated R2 displacement to constrain two basic parameters for the EBF: the near-surface dip angle and the length of time that the fault has been active.

Dip angle of the EBF

The measured R2 displacement, in combination with the horizontal distance separating the R2 depth measurements on the two sides of the fault, provides a lower limit to the dip angle of the fault plane. In the plane of the cross-section of Figure 2d, the vertical R2 displacement occurs over a maximum horizontal distance of 151 m, which is the distance between the two closest stations on the opposite sides of the EBF measured along the A–A′ profile (Figs. 2a and 4b). From this maximum distance, and our preferred R2 depth offset of 810 m with a 1σ uncertainty of 290 m, we determine a minimum apparent dip angle of 79° with a range of 74°–82°. Correcting this apparent dip on the cross-section to the true fault dip, which is the dip normal to the local EBF strike of 40° (Fig. 2a), the near-surface dip on the EBF is >81° ± 3°.

TABLE 1
Measurements of R2 Elevations and Vertical Displacement (m)

R2 Measurement	Mean Using Maximum Probability Models from Figure 1d,e	Standard Deviation (from Fig. S3)
Footwall (east side) elevation	1112	73
Hanging-wall (west side) elevation	298	275
Elevation difference across the fault	813	288

Note. The mean R2 elevations are from depth-migrated RFs using the maximum probability velocity models in Figure 1d,e. These models are constructed by selecting the maximum probability velocity at each depth in 15 m increments from an ensemble of models from the Bayesian inversion (see Kim *et al.*, 2025). The standard deviations are from the mean R2 elevation distributions in Figure S3.

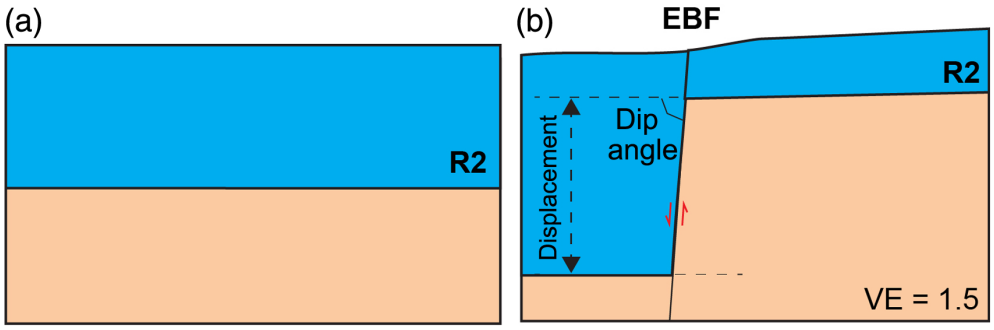

Figure 4. Schematic cartoon showing how we interpret the difference of R2 elevations observed in this study, with a vertical exaggeration (VE) of ~1.5:1. (a) The approximately flat R2 surface before movement on the fault. (b) The displaced R2 surface resulting from normal slip on the East Bench fault (EBF). The vertical R2 offset labeled "displacement" is the displacement of 810 ± 290 m that we measured in this study. The ground surface shown mimics the actual present-day topography. The color version of this figure is available only in the electronic edition.

This steep near-surface dip is typical of young normal fault scarps in unconsolidated materials (McCalpin, 1996). We note that this number is consistent with the 85° ± 5° dip observed at shallow depths (<5 m) in two trenches at the northern end of the EBF (DuRoss *et al.*, 2014; red circle, Fig. 1a). It is also consistent with dips of ~86° and 74° that Liberty *et al.* (2021) interpreted for the top ~300 m of the EBF from seismic reflection profiles crossing this fault at 700 South and 800 South Streets, respectively, after corrections for true dip. The dips of DuRoss *et al.* (2014) and Liberty *et al.* (2021), and our minimum dip of 81°(±3°), are all steeper than the dip of ~70° measured in a bedrock exposure of the Warm Springs fault, the next fault section to the north of the EBF in the Salt Lake City segment of the WFZ (Fig. 1a; Bruhn *et al.*, 1992; McKean and Anderson, 2024). All these near-surface dip angles contrast with the much shallower dip angle of 30°–35° at ~9–12 km depth on the Warm Springs fault, which several studies have inferred from the moment tensor solutions and aftershock distribution for the 2020 M_w 5.7 Magna earthquake (Pang *et al.*, 2020; Kleber *et al.*, 2021; Pechmann *et al.*, 2023). These studies interpreted a listric geometry for the Warm Springs fault, which may extend southward to the EBF.

Activation age of the EBF

We estimated how long the EBF has been slipping to create the observed R2 displacement, using a range of assumptions for how the slip rate may have varied with time. This calculation assumes that before slip began on the EBF, the R2 surface was flat and continuous across the future location of this fault (Fig. 2a). We consider this assumption to be plausible, based on the relatively flat R2 elevations observed on both sides of the fault (Fig. 2d) and the interpretation of R2 as a sedimentary horizon separating semi-consolidated Tertiary sediments from underlying consolidated Tertiary sedimentary rocks.

Text S1 and Table S1 summarize slip-rate estimates for the EBF, which come from two paleoseismic trenching sites (Fig. 1a): the Penrose Drive site (DuRoss *et al.*, 2014; DuRoss and Hylland, 2015) and the Dresden Place site (Garr, 1986; Machette *et al.*, 1992). The Dresden Place slip rates are poorly constrained minimum rates of 0.31 and 0.32 mm/yr for two different late Quaternary time periods. The Holocene Penrose Drive slip rate of 0.5–0.9 mm/yr (DuRoss *et al.*, 2014) is less than DuRoss and Hylland's (2015) preferred slip rate for the whole Salt Lake City segment, which is a middle to late Holocene rate of 1.0–1.4 mm/yr. This difference may be at least partially because the Penrose Drive site is only 0.67 km from the northern end of the EBF, within an en echelon fault stepover and possible displacement transfer zone between the EBF and the Warm Springs fault to the north.

The slip rate on the EBF may have varied with time because the transfer of slip to this fault section from the older FF along the range front may have been gradual and is not necessarily complete. Hence, we assume two simple end-member models for the slip-rate history on the EBF to determine a plausible range of ages for the initiation of slip on this fault. For both models, we assume that the current EBF slip rate is DuRoss and Hylland (2015) preferred average slip rate for the Salt Lake City segment as a whole, which is 1.2 ± 0.2 mm/yr (1σ uncertainty). We propagate errors considering that our R2 displacement measurement and the assumed slip rate are independent of each other (Lee and Forthofer, 2006). Our first model is a step function model in which the transfer of slip from the FF to the EBF fault occurs instantaneously. In this model, the time interval since slip began on the EBF is simply 810 ± 290 m/$(1.2 \pm 0.2 \times 10^{-3}$ m/yr$) = 0.7 \pm 0.3$ Ma. Although this model is unrealistic, it provides a minimum age for the EBF. In our second model, we assume that the slip rate on the EBF increases linearly from the time that slip begins until the present. In this case, the average slip rate on the fault during the time that it is active is half of the current slip rate, and the estimated EBF age is 1.4 ± 0.5 Ma. We consider it unlikely that the slip transfer from the FF to the EBF occurred as gradually as in the linear model. However, this model provides a reasonable upper limit to the age of the EBF. Note that even though the current slip rate that we are assuming for the EBF is an average rate over the last 7.7 ka (DuRoss and Hylland, 2015), this time period is only ~1% of the minimum age of the fault and is therefore negligible. Our estimated age

range for the EBF fault of 0.7 ± 0.3 to 1.4 ± 0.5 Ma is compatible with the qualitative assessment of Personius and Scott (1992) that "The height of these larger [40–50 m] scarps along the EBF suggests surface faulting along the EBF during much of the middle and late Quaternary." Importantly, our estimated maximum age for the EBF is younger than the likely age of the R2 discontinuity, which is in Tertiary basin fill sediments and therefore older than 2.6 Ma.

Future applications of RFs for fault studies

Detection of the sharp displacement of the R2 discontinuity using RFs from the linear array data opens up the possibility for future studies of fault geometry, slip rate, and age using dense seismic arrays. For example, observations of the variations in R2 offsets along the EBF would provide some important clues into how the slip transfer from the FF to the EBF developed over time. Temporary geophone deployments could also be used to obtain detailed maps of R2 depths throughout the SLB and other sedimentary basins in the Wasatch Front region, which would improve analyses of ground shaking hazards. In this region, due to a high degree of urbanization, it is easier, less invasive, and more cost-effective to determine R2 depths with the RF method than with drilling or active seismic source methods. Finally, RFs from temporary geophone deployments across faults in the Wasatch Front region and elsewhere could potentially yield information on fault dips, displacements, slip rates, and/or duration of faulting. The success of such studies would depend on the existence of detectable impedance contrasts that can be correlated across the fault and/or dated, plus the availability of any other necessary information, such as, in the case of our study, a slip rate.

Careful consideration is required while utilizing RFs to investigate faults and sedimentary basin structures. First, it should be ensured that the interpreted peaks are robust. The possibility of the first large peak being the *PpPs* phase instead of the *Ps* phase is discussed in Kim *et al.* (2025). In this study, we ensured the lack of frequency dependence in the RF peak delay times and the lack of a smaller peak preceding the peak that we are interpreting. Second, a reliable velocity model must be chosen to transform the RFs from the time domain to the depth domain. In this study, we used recent velocity models developed from in situ seismic observations (Gkogkas *et al.*, 2021; Kim *et al.*, 2025). Conversely, to some extent, we can use RFs to evaluate the accuracy of the velocity model. The difference in R2 elevation between our velocity models for the two sides of the EBF, ~600 m, accounting for a station elevation difference of ~100 m (Fig. 1d,e), is within the uncertainty range of the R2 displacement from the RF migration (Table 1), showing that the RFs and the velocity models are reasonably consistent.

Summary

In this study, we used *Ps* converted phases in teleseismic RFs, combined with local velocity models, to image an 810 m vertical bedrock offset caused by movement on the EBF. Because the *Ps* phase is generated at the relatively shallow boundary between the bedrock and the overlying low V_S semi-consolidated sediments, the phase conversion points are almost directly beneath the station locations, which provides good lateral resolution. The RFs show that the 810 ± 290 m vertical offset across the fault occurs over a maximum distance of 157 m, the distance between the two closest stations to the surface trace on the footwall and hanging wall. From this information, we calculate a minimum near-surface fault dip of 81° ± 3°. In addition, from the bedrock offset, assuming a current slip rate of 1.2 ± 0.2 mm/yr from paleoseismic studies and a range of scenarios for the slip-rate transfer from the FF to the EBF, our best estimate for when the transfer began is 0.7–1.4 Ma. We envision more applications of the RF method to map fault-related displacements in the urbanized SLB and elsewhere in the region.

Data and Resources

The 2018 linear array data can be found at doi: 10.7914/SN/9H_2018 (Lin and Kim, 2018) and can be obtained from the EarthScope Consortium's Seismological Facility for the Advancement of Geoscience Data Management Center (SAGE DMC; https://ds.iris.edu/ds/nodes/dmc, last accessed December 2025). The velocity models used in the migration can be found in the supplemental material and the Zenodo Repository at doi: 10.5281/zenodo.14010756 (Kim, 2024) and doi: 10.5281/zenodo.17787625 (Kim, 2025). The supplemental material for this article includes Figures S1–S3, Text S1, and Table S1.

Declaration of Competing Interests

The authors acknowledge that there are no conflicts of interest recorded.

Acknowledgments

This study was supported by the U.S. Geological Survey Earthquake Hazards Program, Award Number G23AP00021. H. Kim and F.-C. Lin also acknowledge support from the National Science Foundation project EAR 1753362. Utah Geological Survey staff members Greg McDonald, Stephanie Carney, and Stefan Kirby improved this article through their reviews. Comments from an anonymous reviewer and Christopher B. DuRoss helped improve the article. The authors appreciate the work of the student volunteers who helped install the nodes and are thankful to the residents of the Salt Lake Valley area who agreed to host a seismometer for research.

References

Agostinetti, N. P., F. Martini, and J. Mongan (2018). Sedimentary basin investigation using receiver function: An East African rift case study, *Geophys. J. Int.* **215,** no. 3, 2105–2113, doi: 10.1093/gji/ggy405.

Agrawal, S., C. M. Eakin, and J. O'Donnell (2022). Characterizing the cover across South Australia: A simple passive-seismic method for estimating sedimentary thickness, *Geophys. J. Int.* **231,** no. 3, 1850–1864, doi: 10.1093/gji/ggac294.

Allam, A. (2020). Response to the Mar 18, 2020 M 5.7 Magna, UT Earthquake [Data set], *International Federation of Digital Seismograph Networks*, doi: 10.7914/SN/2A_2020.

Anderson, Z. W., A. P. McKean, and A. W. Yonkee (2024). Interim geologic map of the Fort Douglas quadrangle, Salt Lake, Davis, and Morgan Counties, Utah, *Utah Geol. Surv. Open-File Rept. 767*, 32 pp., 2 plates, scale 1:24,000, doi: 10.34191/OFR-767.

Arnow, T., and R. E. Mattick (1968). Thickness of valley fill in the Jordan Valley east of the Great Salt Lake, Utah, *U.S. Geol. Surv. Profess. Pap. 600-B*, B79–B82, available at https://pubs.usgs.gov/pp/0600b/report.pdf (last accessed December 2025).

Berg, E. M., F.-C. Lin, V. Schulte-Pelkum, A. Allam, H. Qiu, and K. Gkogkas (2021). Shallow crustal shear velocity and *Vp*/*Vs* across southern California: Joint inversion of short-period Rayleigh wave ellipticity, phase velocity, and teleseismic receiver functions, *Geophys. Res. Lett.* **48,** e2021GL092626, doi: 10.1029/2021GL092626.

Biondi, E., J. Castellanos, and R. Clayton (2024). Imaging urban hidden faults with ambient noise recorded by dense seismic arrays, *Seismol. Res. Lett.* **95,** 2280–2289, doi: 10.1785/0220230408.

Bruhn, R. L., P. R. Gibler, W. Houghton, and W. T. Parry (1992). Structure of the Salt Lake segment, Wasatch normal fault zone: Implications for rupture propagation during normal faulting, in *Assessment of Regional Earthquake Hazards and Risk Along the Wasatch Front, Utah, U.S. Geol. Surv. Prof. Pap., 1500*, P. L. Gori and W. W. Hays (Editors), U.S. Government Printing Office, Washington, D. C., H1–H25.

Clark, D. L., C. G. Oviatt, and D. A. Dinter (2020). Geologic map of the Tooele 30′ × 60′ quadrangle, Tooele, Salt Lake, and Davis Counties, Utah, *Utah Geol. Surv. Map 284DM*, 48 pp., 2 appendices, 4 plates, scale 1:62,500, doi: 10.34191/M-284DM.

Cunningham, E., and V. Lekic (2019). Constraining crustal structure in the presence of sediment: A multiple converted wave approach, *Geophys. J. Int.* **219,** no. 1, 313–327, doi: 10.1093/gji/ggz298.

Dueker, K. G., and A. F. Sheehan (1997). Mantle discontinuity structure from midpoint stacks of converted P to S waves across the Yellowstone hotspot track, *J. Geophys. Res.* **102,** no. B4, 8313–8327, doi: 10.1029/96JB03857.

DuRoss, C. B., and M. D. Hylland (2015). Synchronous ruptures along a Major Graben-Forming fault system: Wasatch and West Valley fault zones, Utah, *Bull. Seismol. Soc. Am.* **105,** no. 1, 14–37, doi: 10.1785/0120140064.

DuRoss, C. B., M. D. Hylland, G. N. McDonald, A. J. Crone, S. F. Personius, R. D. Gold, and S. A. Mahan (2014). Holocene and latest Pleistocene paleoseismology of the Salt Lake City segment of the Wasatch fault zone, Utah, at the Penrose Drive trench site, in *Evaluating Surface Faulting Chronologies of Graben-Bounding Faults in Salt Lake Valley, Utah––New Paleoseismic Data from the Salt Lake City Segment of the Wasatch Fault Zone and the West Valley Fault Zone––Paleoseismology of Utah*, C. B. DuRoss and M. D. Hylland (Editors), Vol. 24, Utah Geological Survey Special Study 149, 1–39, 6 appendices, 1 plate, CD.

DuRoss, C. B., S. F. Personius, A. J. Crone, S. S. Olig, M. D. Hylland, W. R. Lund, and D. P. Schwartz (2016). Fault segmentation: New concepts from the Wasatch fault zone, Utah, USA, *J. Geophys. Res. Solid Earth* **121,** 1131–1157, doi: 10.1002/2015JB012519.

Ehlers, T. A., S. D. Willett, P. A. Armstrong, and D. S. Chapman (2003). Exhumation of the central Wasatch Mountains, Utah: 2. Thermokinematic model of exhumation, erosion, and thermochronometer interpretation, *J. Geophys. Res.* **108,** no. B3, doi: 10.1029/2001JB001723.

Garr, J. D. (1986). Findings of fault investigation at the Dresden Apartment Development, 550 South 900 East, Salt Lake City, Utah, *Technical Rept. Delta Job No. 1729A*, Delta Geotechnical Consultants, available at https://geodata.geology.utah.gov/pages/download.php?direct=1&noattach=true&ref=477&ext=pdf&k= (last accessed December 2025).

Gkogkas, K., F.-C. Lin, A. A. Allam, and Y. Wang (2021). Shallow damage zone structure of the Wasatch fault in Salt Lake City from ambient-noise double beamforming with a temporary linear array, *Seismol. Res. Lett.* **92,** no. 4, 2453–2463, doi: 10.1785/0220200404.

Gurrola, H., J. B. Minster, and T. Owens (1994). The use of velocity spectrum for stacking receiver functions and imaging upper mantle discontinuities, *Geophys. J. Int.* **117,** 427–440.

Hatem, A. E., C. M. Collett, R. W. Briggs, R. D. Gold, S. J. Angster, P. M. Powers, E. H. Field, M. Anderson, J. Y. Ben-Horin, T. Dawson, *et al.* (2022). Earthquake geology inputs for the U.S. National Seismic Hazard Model (NSHM) 2023 (western US) (ver. 2.0, February 2022), *U.S. Geol. Surv. data release*, doi: 10.5066/P9AU713N.

Hill, J., H. Benz, M. Murphy, and G. T. Schuster (1990). Propagation and resonance of SH waves in the Salt Lake Valley, Utah, *Bull. Seismol. Soc. Am.* **80,** 23–42.

Kim, H. J. (2024). Velocity models from "Seismic Imaging of the Salt Lake Basin Using Joint Inversion of Receiver Functions and Rayleigh Wave Data", *Zenodo*, doi: 10.5281/zenodo.14010756.

Kim, H. J. (2025). Velocity model used for migration in "Bedrock Offset Across the Wasatch Fault in Salt Lake City, Utah, from Teleseismic Converted Phases and Its Geologic Implications", *Zenodo*, doi: 10.5281/zenodo.17787625.

Kim, H. J., F.-C. Lin, J. C. Pechmann, C. L. Hardwick, and A. P. McKean (2025). Seismic imaging of the Salt Lake basin using joint inversion of receiver functions and Rayleigh wave data, *J. Geophys. Res. Solid Earth* **130,** e2024JB030927, doi: 10.1029/2024JB030927.

Kleber, E., A. P. McKean, A. I. Hiscock, M. D. Hylland, C. L. Hardwick, G. N. McDonald, Z. W. Anderson, S. D. Bowman, G. C. Willis, and B. A. Erickson (2021). Geologic setting, ground effects, and proposed structural model for the 18 March 2020 M_w 5.7 Magna, Utah, earthquake, *Seismol. Res. Lett.* **92,** 710–724, doi: 10.1785/0220200331.

Langston, C. A. (1979). Structure under Mount Rainier, Washington, inferred from teleseismic body waves, *J. Geophys. Res.* **84,** no. B9, 4749–4762, doi: 10.1029/JB084iB09p04749.

Lee, E. S., and R. N. Forthofer (2006). Strategies for variance estimation, in *Strategies for Variance Estimation*, Second Ed., SAGE Publications, Inc., 23–39, doi: 10.4135/9781412983341.n4.

Lekić, V., and K. M. Fischer (2017). Interpreting spatially stacked *Sp* receiver functions. *Geophys. J. Int.* **210,** no. 2, 874–886, doi: 10.1093/gji/ggx206.

Liberty, L. M., J. St. Clair, and A. P. McKean (2021). A broad, distributed active fault zone lies beneath Salt Lake City, Utah, *Seism. Rec.* **1,** no. 1, 35–45, doi: 10.1785/0320210009.

Lin, F.-C., and H. J. Kim (2018). Salt lake linear nodal array 2018, *International Federation of Digital Seismograph Networks*, doi: 10.7914/SN/9H_2018.

Machette, M. N., S. F. Personius, and A. R. Nelson (1992). Paleoseismology of the Wasatch fault zone: A summary of recent investigations, interpretations, and conclusions, in *Assessment of Regional Earthquake Hazards and Risk Along the Wasatch Front, Utah, U.S. Geol. Surv. Profess. Pap. 1500-A-J*, P. L. Gori and W. W. Hays (Editors), A1–A71.

Magistrale, H., K. B. Olsen, and J. C. Pechmann (2008). Construction and verification of a Wasatch front community velocity model, *U.S. Geol. Surv. Technical Rept. no. HQGR.060012*, Reston, Virginia, 14 pp.

Marsell, R. E. (1969). The Wasatch fault zone in north central Utah, in *Guidebook of Northern Utah*, M. L. Jensen (Editor), Utah Geological and Mineralogical Survey Bulletin, Vol. 82, 125–139, doi: 10.34191/B-82.

Mattick, R. E. (1970). Thickness of unconsolidated to semiconsolidated sediments in Jordan Valley, Utah, *U.S. Geol. Surv. Profess. Pap. 700-C*, C119–C124, available at https://pubs.usgs.gov/pp/0700c/report.pdf.

McCalpin, J. P. (1996). Paleoseismology in extensional tectonic environments, in *Paleoseismology*, J. P. McCalpin (Editor), Academic Press, San Diego, California, 588 pp.

McKean, A. P. (2020). Geologic map of the Sugar House quadrangle, Salt Lake County, Utah, *Utah Geol. Surv. Map 285DM*, 27 pp., 2 plates, scale 1:24,000, doi: 10.34191/M-285DM.

McKean, A. P., and Z. W. Anderson (2024). Interim geologic map of the Salt Lake City North quadrangle, Salt Lake and Davis Counties, Utah, *Utah Geol. Surv. Open-File Rept. 768DM*, 38 pp., 2 plates, scale 1:24,000, doi: 10.34191/OFR-768DM.

Pang, G., K. D. Koper, M. Mesimeri, K. L. Pankow, B. Baker, J. Farrell, J. Holt, J. M. Hale, P. Roberson, R. Burlacu, *et al.* (2020). Seismic analysis of the 2020 Magna, Utah, earthquake sequence: Evidence for a Listric Wasatch fault, *Geophys. Res. Lett.* **47,** e2020GL089798, doi: 10.1029/2020GL089798.

Parry, W. T., and R. L. Bruhn (1987). Fluid inclusion evidence for minimum 11 km vertical offset on the Wasatch fault, Utah, *Geology* **15,** 67–70.

Pechmann, J. C., K. J. Jensen, and H. Magistrale (2010). Constraints on the near surface seismic velocity structure of the Wasatch front region, Utah, from Sonic log analyses. Abstracts of the annual meeting. *Seismol. Res. Lett.* **81,** no. 2, 284–388, doi: 10.1785/gssrl.81.2.284.

Pechmann, J. C., I. G. Wong, C. B. DuRoss, M. D. Hylland, A. J. Crone, S. F. Personius, A. P. McKean, W. J. Arabasz, D. P. Schwartz, S. S. Olig, *et al.* (2023). A logic tree for the subsurface geometry of the Salt Lake City segment of the Wasatch fault in light of the 2020 Magna, Utah, earthquake, *Proceedings Volume, Basin and Range Earthquake Summit, 17–20 October 2022*, A. I. Hiscock, E. Williams, E. J. Kleber, and S. D. Bowman (Editors), Utah Geological Survey Miscellaneous Publication 177 (electronic poster), Salt Lake City, Utah.

Personius, S. F., and W. E. Scott (1992). Surficial geologic map of the Salt Lake City segment and parts of adjacent segments of the Wasatch fault zone, Davis, Salt Lake, and Utah Counties, Utah (1992), *U.S. Geol. Surv. Misc. Invest. Series Map I-2106*, scale 1:50,000, doi: 10.3133/i2106.

Petersen, M. D., M. P. Moschetti, P. M. Powers, C. S. Mueller, K. M. Haller, A. D. Frankel, Y. Zeng, S. Rezaeian, S. C. Harmsen, O. S. Boyd, *et al.* (2014). Documentation for the 2014 update of the United States national seismic hazard maps, *U.S. Geol. Surv. Open-File Rept. 2014-1091*, 243 pp., doi: 10.3133/ofr20141091.

Petersen, M. D., A. M. Shumway, P. M. Powers, E. H. Field, M. P. Moschetti, K. S. Jaiswal, K. R. Milner, S. Rezaeian, A. D. Frankel, A. L. Llenos, *et al.* (2024). The 2023 US 50-state National Seismic Hazard Model: Overview and implications, *Earthq. Spectra* **40,** no. 1, 5–88, doi: 10.1177/87552930231215428.

Scott, W. E., and R. R. Shroba (1985). Surficial geologic map of an area along the Wasatch fault zone in the Salt Lake Valley, Utah, *U.S. Geol. Surv. Open-File Rept. 85-448*, 18 pp., doi: 10.3133/ofr85448.

Shibutani, T., T. Ueno, and K. Hirahara (2008). Improvement in the extended-time multitaper receiver function estimation technique, *Bull. Seismol. Soc. Am.* **98,** no. 2, 812–816, doi: 10.1785/0120070226.

Stephenson, W. J., J. K. Odum, R. A. Williams, J. H. McBride, and I. Tomlinson (2012). Characterization of intrabasin faulting and deformation for earthquake hazards in southern Utah Valley, Utah, from high-resolution seismic imaging, *Bull. Seismol. Soc. Am.* **102,** no. 2, 524–540, doi: 10.1785/0120110053.

U.S. Geological Survey and Utah Geological Survey (2023). Quaternary fault and fold database for the United States, available at https://www.usgs.gov/natural-hazards/earthquake-hazards/faults (last accessed May 2023).

Wang, X., Z. Zhan, M. Zhong, P. Persaud, and R. W. Clayton (2021). Urban basin structure imaging based on dense arrays and Bayesian array-based coherent receiver functions, *J. Geophys. Res.* **126,** e2021JB022279, doi: 10.1029/2021JB022279.

Wong, I. G., W. R. Lund, C. DuRoss, P. Thomas, W. Arabasz, A. J. Crone, M. D. Hylland, N. Luco, S. S. Olig, J. C. Pechmann, *et al.* (2016). *Earthquake Probabilities for the Wasatch Front Region in Utah, Idaho, and Wyoming*, Miscellaneous Publication 16-3 Utah Geological Survey, Utah Department of Natural Resources.

Zeng, Q., F.-C. Lin, and A. A. Allam (2022). 3D shear wave velocity model of Salt Lake Valley via Rayleigh wave ellipticity across a temporary geophone array, *Seism. Rec.* **2,** no. 2, 127–136, doi: 10.1785/0320220016.

Zhu, L., and H. Kanamori (2000). Moho depth variation in southern California from teleseismic receiver functions, *J. Geophys. Res.* **105,** no. B2, 2969–2980, doi: 10.1029/1999JB900322.

Manuscript received 14 July 2025
Published online 15 December 2025